Pis'ma v ZhETF, vol. 97, iss. 12, pp. 793 – 799 © 2013 June 25

Human cervical carcinoma detection and glucose monitoring in blood micro vasculatures with swept source OCT

H. Ullah[+*1)], *E. Ahmed*[*], *M. Ikram*[+]

[+]*Department of Physics and Applied Mathematics, Pakistan Institute of Engineering and Applied Sciences, 45650 Islamabad, Pakistan*

[*]*Department of Physics, Bahauddin Zakariya University, Multan, Pakistan*

Submitted 21 March 2013
Resubmitted 20 May 2013

We report a pilot method i.e. speckle variance (SV) and structured optical coherence tomography to visualize normal and malignant blood microvasculature in three and two dimensions and to monitor the glucose levels in blood by analyzing the Brownian motion of the red blood cells. The technique was applied on nude live mouse's skin and the obtained images depict the enhanced intravasculature network forum up to the depth of ~ 2 mm with axial resolution of $\sim 8\,\mu$m. Microscopic images have also been obtained for both types of blood vessels to observe the tumor spatially. Our SV-OCT methodologies and results give satisfactory techniques in real time imaging and can potentially be applied during therapeutical techniques such as photodynamic therapy as well as to quantify the higher glucose levels injected intravenously to animal by determining the translation diffusion coefficient.

DOI: 10.7868/S0370274X13120084

1. Introduction. Many qualitative and quantitative spectroscopic techniques have been used for biotissues diagnostics [1–3] with their own set of advantages and disadvantages [4]. For example, excisional biopsy can alter the original morphology and always can iatrogenic trauma [5]. Hence, using non-invasive optical imaging modalities such as optical fluorescence microscopy, computing tomography, optical diffuse tomography and optical coherence tomography (OCT) etc. which are capable to construct 2D or 3D images of tissue surfaces as well as the interior of the body [6–9] can improve the diagnostics of diseases. Optical fluorescence cryomicrotome images have been used to reconstruct 3D coronary vasculature using point spread function (PSF) by extracting the vascular anatomy (phantom) for light scattering simulations in the tissue. The disadvantage includes when modeling without correcting for the optical blurring, resulted in 42.9% error on average for the vessel [8]. During the past 15 years, OCT has been proved to be a new noninvasive imaging method on micron-scale by measuring of backscattered infrared light [10]. The reason for OCT's popularity included its high resolution cross-sectional imaging capability (*in situ, in vitro* and in *vivo*) [11]. OCT's parameters like image depth, resolution, contrast, and acquisition rate etc. imposed with a source power that does not damage the tissue [12, 13] are crucial to be considered in different biomedical applications. For example, OCT is currently well suited to hemodynamics of the microvasculature bed study with the penetration depth $\sim 1-2$ mm as compared to microscopy [14] at resolution of $2-30\,\mu$m [15]. OCT also has been used *in situ* determination of the intrinsic optical attenuation coefficient of atherosclerotic tissue components within regions of interest (ROI) differentiating between various plaque types within the vessel wall [9]. In ophthalmology, spectral domain OCT (SD-OCT) or swept source OCT (SS-OCT) offer the segmentation of retinal vessels by using complimentary information from fundus photographs [16]. The attractive feature of the OCT is that it does not require any contact to object and is nondestructive because light waves are used for investigations.

In this work, we present a pilot method using the structural and speckle variance (SV-OCT) subsequently applied primarily to image soft biological tissues of blood vessels in the normal and tumor induced mice. Although it was challenging due to the sensitivity of the technique to longitudinal motion but the *in vivo* measurement for anesthetized mouse with swept source (SS-OCT) was carried out. The results obtained with this useful technique have potential application in dermatology, glucose monitoring in blood analyzing Brownian motion of erythrocytes under the phenomena of DLS or ballistic photon scattering fluids in M-mode imaging, and real time imaging during photodynamic therapy. Therefore, we have implemented on of the above men-

[1)]e-mail: hafeezullah79@gmail.com

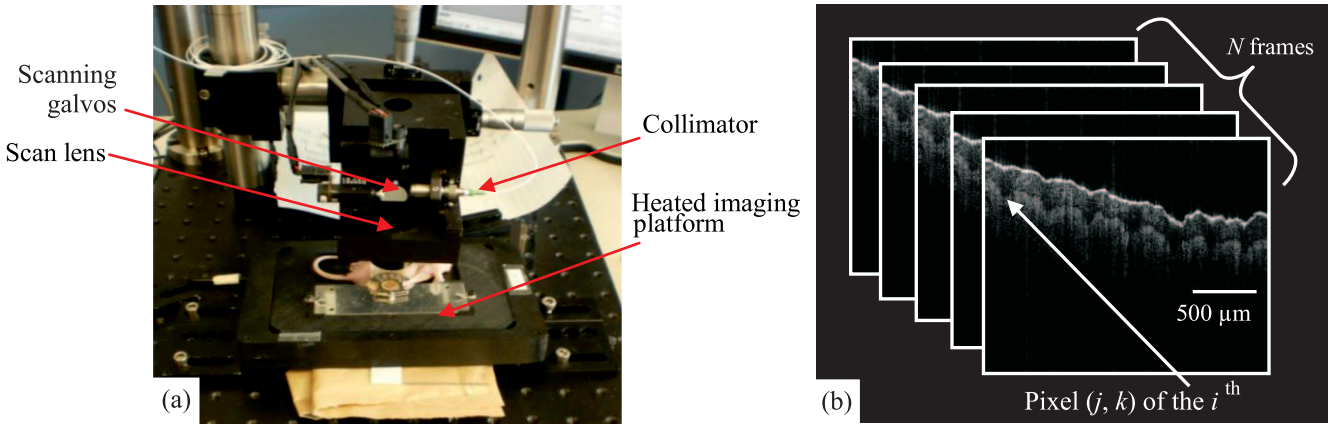

Fig. 1. (a) – A nude mouse with WCM implanted to image blood vessels with SV-OCT under the scanning head of OCT system. (b) – A conceptual diagram of an acquired speckle variance data set of N frames and corresponding indices used to label the frame (i), transverse pixel location (j) and the axial pixel location (k)

tioned applications i.e. to quantify the glucose level in prior to glucose injection mouse as a base line. We have investigated the translational relaxation or decorrelation time in Brownian motion rather rotational relaxation. The SV-OCT images have been used to visualize the blood vessels in three dimensions so that light can be directly focused on the microvasculature for OCT signal. The idea of quantification of the salt levels in simple stagnant blood has been translated successfully for *in vivo* case scenario for non-injected glucose animals [2]. This quantitative data will be proved very helpful in translating the *in vitro* study into *in vivo* environment for measurements of higher glucose concentration intravenously into the animal.

2. Materials and Methods. *2.1. Sample preparation: animal model.* The SV algorithm was applied to image the blood vessels of normal and tumor induced mice (in vivo). A dorsal skin-fold windows chamber model (WCM) was applied on anesthetized mouse under institutional laws of Princess Margret Hospital, Toronto approved by the University Health Network Animal Resource Centre. The mouse before surgery was anesthetized with a ketamine–xylazine (90–10 mg/kg) mixture. A 10 mm diameter region of skin was placed between the titanium plates of WCM. A 12 mm diameter and 250 μm thick cover slip was used to protect the exposed fascia and vasculature. After recovery of the animal from surgery, OCT imaging was performed by fixing the WCM into the removable light weight aluminum plate to keep the animal at 37 °C. The mice were induced by tumor, ME180 human cervical carcinoma cells transfected with the DsRed2 fluorescent protein. After injection the tumor into the fascia we waited for one week so that tumor would grow before imaging. The purpose of fluorescent protein was to enhance the visibility of tumor through microscope for subsequent coregistration of fluorescent and SV-OCT images.

2.2. Swept source OCT imaging system. OCT images data were obtained from 36 kHz SS-OCT system described earlier in our recent work [2]. Briefly, it consists of frequency domain mode locking (FDML) fiber-ring laser source comprising of polygon-based tunable filter. The coherence length and spectral sweeping range were 6 mm and 112 nm, respectively, at a fundamental wavelength of 1310 nm. The axial resolution in tissue and the average output power of the system were 8 μm and 50 mW. The coherence length 6 mm is determined exclusively from sweeping resolution of laser source that was 2 nm.

Our OCT system uses a broadband light source and resolves the scattered signal by dispersing the signal into many k-values (elementary emanating waves). In SS-OCT, the laser source does not directly sweep linearly into k-space but rather time space. So, first the recalibration is required from the linear-in-time data to linear-in-k data. The common approach to achieve this goal is to fix the pathlength for interferometeric signal. Hence the SS-OCT's signal in k-space can be written as

$$I(k) \approx S(k)\cos(2knz_0), \qquad (1)$$

where, $S(k)$ is the incident intensity for each k-value used (the swept source spectrum) and z_0 – offset distance between reference plane and object surface. For k, a positive integral multiple of $\pi/2nz_0$ the maxima and minima of this equation are produced that specify the location of equally

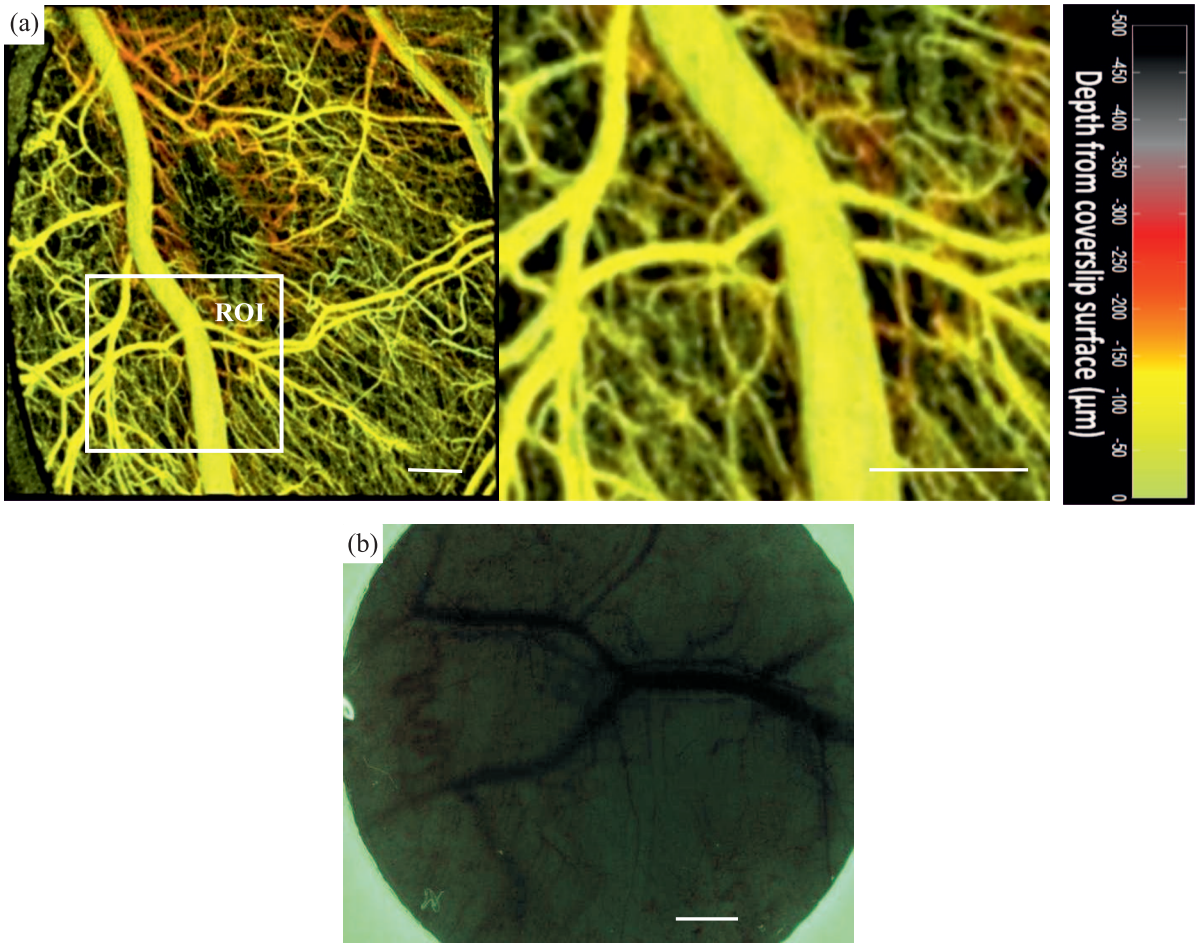

Fig. 2. (a) – SV-OCT microvasculature image of a normal mouse in WCM, a low bulk tissue motion situation with gate length $N = 8$. This shows a 3D processed image of blood microvasculature to distinguish the individual blood vessels. Dimensions: ($6400 \times 1520 \times 512$, pixels) and/or ($6 \times 6 \times 2.2\,\mathrm{mm}^3$). The ROI is represented with magnification and depth encoded color bar used to specify the depth of the vessel. Scale bar: $250\,\mu$m (b) a microscopic z-stack image displaying the micro vessels with high lateral resolution but minimal axial information. Dimension: ($6.2 \times 6.2\,\mathrm{mm}^2$) and Scale bar: 1mm (color online)

spaced k-values regardless of the temporal dependence of the sweep. A photograph of scanning head with animal under measurements is shown in Fig.1a.

2.3. 3D image processing algorithm: speckle variance (SV-OCT). The interframe OCT fluid contrast algorithm termed as SV-OCT is based on the idea that the image speckle/texture of relatively solid regions will persist between consecutive images, whereas speckle will show greater inter-image speckle washout in regions of greater fluidity [17] was designed by our research group (mainly by Dr. Adrian Mariampillai [18]) at Princess Margret hospital, Toronto, Canada. The algorithm for generation of speckle variance images of OCT data needs to calculate the variance of pixels from a set of N, B-mode images (N is gate length), acquired from the same spatial location

$$SV_{ijk} = \frac{1}{N}\sum_{i=1}^{N}\left(I_{ijk} - \frac{1}{N}\sum_{i=1}^{N} I_{ijk}\right)^2, \qquad (2)$$

where i, j and k are indices for the frame (up to N), transverse, and axial pixels, and I is the corresponding pixel intensity value at the imaging speeds of 20 frames per second. A more clearly schematic representation of the data set and pixel indices for three dimensional frames stacking according to Eq. (2) is shown in Fig. 1b.

2.4. Brownian motion and M-mode imaging of in vivo mouse. A particle executing Brownian (random) motion in a liquid has squared displacement $\langle \mathbf{r}^2 \rangle$ and for diffusing particle is given by [19]

$$\langle \Delta r^2(t) \rangle = 6 D_T \tau_T. \qquad (3)$$

Here D_T (translation diffusion coefficient) and τ_T (translational relaxation or decorrelation time) are related by the following formula [19],

$$\tau_T = \frac{1}{2k^2 D_B}. \quad (4)$$

This gives us the diffusion coefficient extracted from the translations decorrelation time. The decay is exponential in nature [2]. To get M-mode data, we selected the blood vessel of diameter $\sim 160\,\mu$m at depth of $\sim 55\,\mu$m from top surface of the tissue and can be seen in SV-OCT microvasculature image (Fig.2a). The data from three ROIs was averaged for each animal because of the little bit difference in decorrelation time due to difference on flowing speed or shear effect. The measurement scheme for *in vivo* M-mode measurements was same as described recently by our group [2]. We examined a total of 5 animals in this experiment. The obtained M-mode OCT data was processed to calculate the autocorrelation function (ACF) from power spectrum, $P(\omega)$ by means of Fourier transformation using Weiner–Khinchin theorem [2, 20].

A double exponential fit function $f_1 = B^* \exp(-t/\tau'_T) + C^* \exp(-t/\tau'_R)$ was applied on the ACF because of the asymmetric shape of RBCs. From above fitted function we got both τ'_T and τ'_R are indeed occurring in dynamic light scattering for *in vivo* case because of transitional and rotational motion but we processed the data for translational diffusion coefficient rather rotational. This was decided after examining the B/C ratio (relative importance of translational relaxation versus rotational relaxation) which was found to be ~ 3.85 that strongly recommends that translational relaxation is dominant over rotational motion.

3. Results. Figure 2a shows a blood vessels image of normal nude mouse obtained with SV-OCT. This shows a 3D processed image of blood microvasculature to distinguish the individual blood vessels with dimensions of $6 \times 6 \times 2.2\,\text{mm}^3$. Figure 2b shows a light microscopic image displaying the micro vessels with high lateral resolution with dimension of $6.2 \times 6.2\,\text{mm}^2$ in WCM. Figure 3a shows blood vessels having tumor induced in nude mouse obtained with SV-OCT with dimensions of $6 \times 6 \times 2.2\,\text{mm}^3$. This reflects the capability of SV-OCT to map the abnormalities in blood vessels that could be implemented in diabetes having tumor diseases. Figure 3b shows corresponding maximum-intensity projection image of a fluorescence confocal z-stack image obtained using 500 kD Fluorocein labeled dextran with dimensions of $2.2 \times 2.2\,\text{mm}^2$.

Figure 4a gives an original structured OCT image in which different layers under laying the fascia can be observed but the image is not clearer for diagnostic point of view. Anyhow, we get sufficient information up to this limit for layers differentiations. The corresponding OCT signal decaying exponentially for nude female mouse skin *in vivo* is shown in Fig.4b. The first peak is due to the backscattering of cover glass and second peck represents the surface of the tissue. Figure 4c shows the colorized image with efficient noise removed with code written by us for colorization in visual C^{++} resulting in an easy analysis of the image [21-22].

The SV-OCT image used to select the ROI for *in vivo* study of glucose monitoring in five animals with the help of M-mode imaging the average value of D_T was yield $\sim 5.85 \cdot 10^{-14}\,\text{m}^2/\text{s}$ (Table). This value was $\sim 10\%$ different from theoretical value of diffusion coefficient ($5.85 \cdot 10^{-14}\,\text{m}^2/\text{s}$ vs. $6.50 \cdot 10^{-14}\,\text{m}^2/\text{s}$ [23]). This difference might be originated due to forced convection, shear effect and technique employed for measurements. As the technique used in [23] to determined D_T was diffuse wave spectroscopy (DWS) applied *ex vivo* on porcine kidney model at controlled arterial pressure and flow. Figure 2a provides clear 3D image of glucose free mouse to visualize the blood microvessells for easy selection of the ROI to obtain M-mode data. Thus, we get the threshold measurement to quantify glucose levels in case of injected higher glucose concentrations intravenously.

4. Discussions. The SV algorithm represented in Fig. 1b provides an interfame algorithm to mitigate the bulk tissue motions so that phase sensitive images can be envisioned with high precisions. Figure 2a shows a reconstructed image of the vascular structure in the skin of mouse using SV-OCT analysis. This shows a 3D processed image with Eq. (2) of blood microvasculature to distinguish the individual blood vessels in depth with axial resolution of $\sim 8\,\mu$m and lateral resolution of $\sim 13\,\mu$m. In Fig. 2b, we see that light microscopic image of blood vessels presents higher lateral resolution but low axial information. Our reconstruction for 3D view from structured images gives full map (axially) of field of view and has capabilities to visualize the individual vessels up to the depth of $\sim 2.2\,$mm. Because in SV algorithm, we have segmented out the higher interframe variance (@20 frames per image) possibly due to dynamic scatterers such as RBCs in blood vessel of various diameters. The size and depth of individual vessel is given by the color bar provided on the right hand side of the ROI image.

SV algorithm has potential application to demonstrate the life morphology by identifying the dense

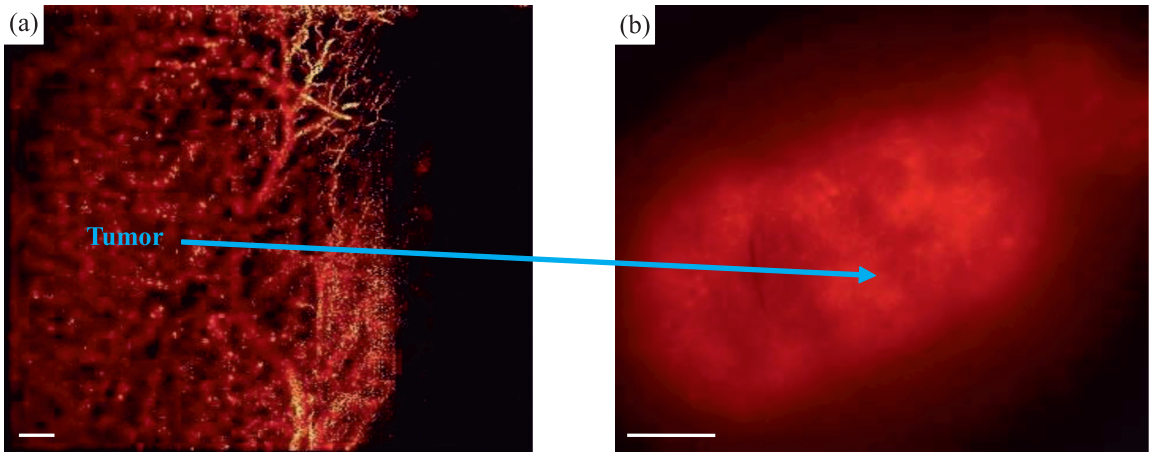

Fig. 3. (a) – Blood vessels of nude tumor induced mouse obtained with SV-OCT. This shows a 3D processed image of blood microvasculature to distinguish the individual blood vessels. Dimensions: ($6400 \times 1520 \times 512$, pixels) and/or ($6 \times 6 \times 3.2\,\mathrm{mm}^2$) and Scale bar: $250\,\mu$m and (b) corresponding maximum-intensity projection image of a fluorescence confocal z-stack obtained using 500 kD Fluorocein labeled dextran. Dimensions: ($2.2 \times 2.2\,\mathrm{mm}^2$) and Scale bar: $500\,\mu$m (color online)

Summary of Brownian motion analysis results in dynamic light scattering regime including translational decorrelation time, translational diffusion coefficient and r^2-values for all five animals

Animals	Translational decorrelation time, ms	Translational diffusion coefficient, $10^{-14}\,\mathrm{m}^2/\mathrm{s}$	r^2-value
Animal 1	38.20	1.02	0.93
Animal 2	44.00	6.68	0.95
Animal 3	48.80	6.03	0.98
Animal 4	46.70	6.30	0.99
Animal 5	52.20	9.20	0.96
Average	45.98	5.85	0.96

branching of microvasculature both in normal and malignant skins. The microvasculature system undergoes a significant change in the density and shape after inducing the tumor i.e. vascular plexus of blood circulation is perturbed and thrombosis can be seen (Figs. 2 and 3). This hierarchical network in hemodynamic has interesting potential application like monitoring of analytes in our recent study of glucose quantification with M-mode OCT and SV-OCT [2] before and after injection of glucose intravenously. This would change the density of vessels after changing in the shape of erythrocytes when glucose injected in blood vessels. Hence, the visualization of vasculature with SV-OCT can provide valuable information underneath the skin in diabetes either cancerous or non-cancerous.

The blood borne glucose provides the constant supply to cerebral metabolism [24]. The glucose transported to nerve tissue is separated by functional barrier (the blood-brain barrier, BBB), a characteristic of the cerebral endothelium. To know about its metabolic regulation and developmental expression in the BBB [25], the vasculature net is necessary to visualize in any of the conditions like normal glucose supply, hyperglycemia, and hypoglycemia. Thus, we provide a basic route to study modulations in micro blood vessels both in 2D and 3D imaging with structures OCT and SV-OCT images. Another application of this study is the understanding of the role of mechanical factors in cardiovascular development [17] depending on the apparent morphological difference between the normal and abnormal primitive vascular plexus. The limitations of SV-OCT include sensitivity for high intensity fluctuations due to shadowing effect [26], because, the interframe variance is produced due to its sensitivity to bulk tissue motion (BTM). This BTM was minimized by using WCM in this study or a high speed using imaging system can be used i.e. high A-scan acquisition speed to ensure sufficient number of acquired frames for calculation of speckle decorrelation. Another cause of this variance in the intensity of each voxel might be the shape of the scattering particles such

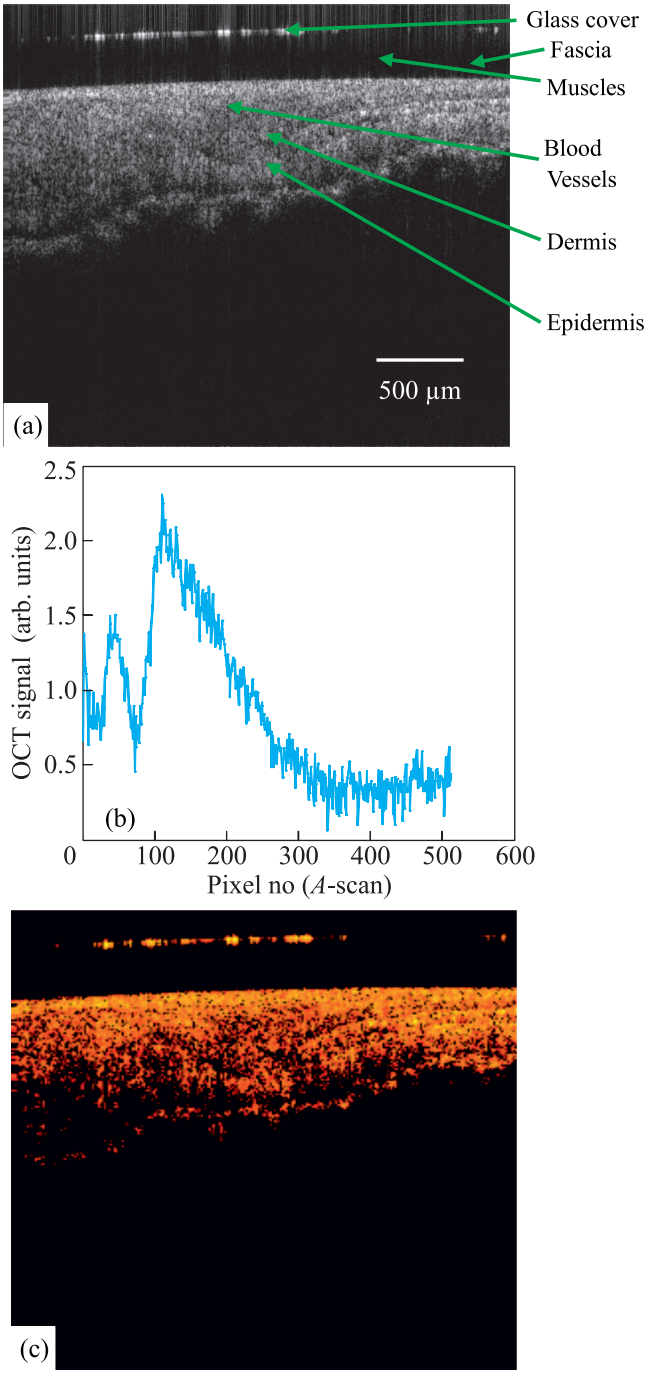

Fig. 4. (a) – Original gray scale structured OCT image of mouse skin. Dimensions (640 × 512 pixels) pixels, where 1 pixel = 3.9 μm (color online). (b) – The OCT signal decaying exponentially for nude female mouse skin *in vivo*. The first peak is due to the backscattering of cover glass and second peck represents the surface of the tissue. The depth contains a total of 512 pixels in ∼3 mm depth, again 1 pixel ∼3.9 μm. (c) – Noise removed hard segmented OCT image with dimensions (256 × 256) pixels, where 1 pixel = = 3.9 μm

as red blood cells, keratinocyte like Starum Granulosum, Starum Spinosum, and Stratum Basale in epidermis lie in different shapes, sizes and refractive indexes [6].

It is worth to mention that OCT has increased dramatically the efficacy of preclinical studies to monitor the disease on real time. During imaging the live animals, anesthesia is much necessary to minimize the motion artifacts (i.e. to restrain the animal) and is important challenge in contrast to human studies. The injection of anesthesia drug to animal reasonably changes the animal's physiology that can export more or less different data to imaging device which is much difficult in human beings. The repeated anesthesia, exposure of ionizing radiations and the use of contrast agents and/or imaging biomarkers can also affect the physiology of animal [27] that should be considered during the results analysis.

Therefore, speckle contrast levels in SV-OCT provide a better 3D understanding than original structured unprocessed images for *in vivo* skin. Our *B*-scan swept source method is sufficient and straightforward for transverse sampling of the full speckle pattern in practical implementations. The technique can be applied during photodynamic therapy (PDT) procedure by monitoring the blood vasculature up to a depth of few millimeters in case of superficial tumors [28]. But during PDT, there are multiple tissue reactions post PDT. Our fundamental *in vivo* work of glucose monitoring has a significant application in the patients of hyperglycemia, where, fibrinogen depletion can reduce the blood viscosity after intravenous administration of ancrod. We have reported therefore the reference value of glucose diffusion by measuring diffusion coefficient of healthy animals that can be implemented initially in lab experiments as a non invasive method. Therefore OCT's capability for monitoring glucose in blood vessels of diameters in micron ranges provides the route to enhance the application for further glucose concentration's quantification.

5. Conclusions. The potential application of speckle variance OCT and structured OCT was validated to visualize the skin of live nude mouse. The quantitative metrics developed and implemented in this study uncover and measure vascular characteristics from 3D SV-OCT images. Our method demonstrates that SV-OCT is applicable for microvasculature detection in normal and tumor induced vessels within WCM and carries more information than structured OCT. That is more accurate and unique representation of the vascular structure underlying biology of vasculature development and response. For *in vivo* study of glucose

monitoring the RBCs can have the same dynamics as are used in flowing blood (*in vitro* study) through the capillary tube to reinforce the concept that RBCs are only asymmetrical particles that cause the change in the OCT signal due to Brownian motion underlying the DLS. Thus, the translational diffusion coefficients have been determined to provide a base line in this perspective to image the deformation in microvasculature for further higher glucose levels.

This research was supported by Higher Education Commission Pakistan, Islamabad, Pakistan. One of the authors, Dr. Hafeez Ullah highly acknowledges Dr. Prof. Alex Vitkin, Leigh Conroy, Adrian Mariampillai, Michael Wood, and Azusa Maeda at Department of Medical Biophysics, University of Toronto, Canada, who allowed and helped him to use the Biophotonics laboratory.

1. A. Lemelle, B. Veksler, I. S. Kozhevnikov et al., Laser Physics Letters **6**, 71 (2009).
2. H. Ullah, G. Gilanie, M. Attique et al., Laser Physics **22**, 1002(2012).
3. S. Oeltze and B. Preim, Medical Imaging, IEEE Transactions on **24**, 540 (2005).
4. N. Sharma and L. M Aggarwal, J Med Phys **35**, 3 (2010).
5. T. Gambichler, G. Moussa, M. Sand et al., Journal of Dermatological Science **40**, 85 (2005).
6. H. Ullah, M. Atif, S. Firdous et al., Laser Physics Letters **7**, 889 (2010).
7. B. Veksler, E. Kobzev, M. Bonesi, and I. Meglinski, Laser Physics Letters **5**, 236 (2008).
8. A. Goyal, J. Lee, P. Lamata et al., Medical Imaging, IEEE Transactions on **32**, 56 (2013).
9. F. J. van der Meer, D. J. Faber, D. M. B. Sassoon et al., Medical Imaging, IEEE Transactions on **24**, 1369 (2005).
10. A. F. Fercher, W. Drexler, C. K. Hitzenberger, and T. Lasser, Reports on Progress in Physics **66**, 239 (2003).
11. M. Atif, H. Ullah, M. Y. Hamza, and M. Ikram, Laser Physics Letters **8**, 629 (2011).
12. J. G. Fujimoto, *Hand book of Optical Coherence Tomography*, MarcelDekker, Inc., N.Y., 2002.
13. Z. Hamdoon, W. Jerjes, T. Upile, and C. Hopper, Photodiagnosis and Photodynamic Therapy **8**, 49 (2011).
14. S. Gu, M. W. Jenkins, L. M. Peterson et al., Developmental Dynamics **241**, 534 (2012).
15. J. G. Fujimoto, Nature Biotechnology **21**, 1361 (2003).
16. H. Zhihong, M. Niemeijer, M. D. Abramoff, and M. K. Garvin, Medical Imaging, IEEE Transactions on **31**, 1900 (2012).
17. N. Sudheendran, S. H. Syed, M. E. Dickinson et al., Laser Physics Letters **8**, 247 (2011).
18. A. Mariampillai, *Development of a high resolution microvascular imaging toolkit for optical coherence tomography*, PhD Thesis, Dept. Med. Biophys. University of Toronto, Toronto, Canada, 2010.
19. B. J. Berne and R. Pecora, *Dynamic Light Scattering with applications to Chemistry, Biology, and Physics*, Dover publications Inc., N.Y., 2000.
20. M. Brezinski, *Optical coherence tomography principles and applications*, San Diego, USA: Elsevier, 2006.
21. M. Attique, G. Gilanie, Hafeez-Ullah et al., PLoS ONE **7**, e33616. doi:10.1371/journal.pone.0033616 (2012).
22. G. Gilanie, M. Attique, Hafeez-Ullah et al., Pattern Recognition Letters (2013).
23. M. Ninck, M. Untenberger, and T. Gisler, Biomed. Opt. Exp. **1**, 1502 (2010).
24. R. Dermietzel, D. Krause, M. Kremer et al., Developmental Dynamics **193**, 152 (1992).
25. A. J. Barber and E. Lieth, Developmental Dynamics **208**, 62 (1997).
26. J. Fingler, D. Schwartz, C. Yang, and S. E. Fraser, Opt. Express **15**, 12636(2007).
27. L. Tremoleda, A. Kerton, and W. Gsell, EJNMMI **2**, 1 (2012).
28. G. Hüttmann, Photodiagnosis and Photodynamic Therapy **8**, 152 (2011).